RSC Advances

RSC Publishing

PAPER

View Article Online
View Journal | View Issue

Cite this: *RSC Advances*, 2013, **3**, 18908

Sol–gel synthesis of defect-pyrochlore structured $CsTaWO_6$ and the tribochemical influences on photocatalytic activity†

Larissa Schwertmann,[a] Michael Wark[ab] and Roland Marschall*[ac]

Received 8th July 2013,
Accepted 5th August 2013

DOI: 10.1039/c3ra42768d

www.rsc.org/advances

The semiconductor mixed oxide photocatalyst $CsTaWO_6$ was prepared *via* an aqueous sol–gel citrate route for the first time. The mild reaction conditions yield smaller primary particle sizes and larger specific surface areas than the conventional solid state reaction. The photocatalytic properties are determined using both photocatalytic terephthalic acid hydroxylation and photocatalytic hydrogen generation. All of the materials described herein generate hydrogen without the addition of a co-catalyst. Due to the initially agglomerated but porous morphology of the sol–gel-derived $CsTaWO_6$, tribochemical treatment *via* short term ball milling has a strong effect on the photocatalytic activities of these materials. Ball milling increases the surface area of the materials, leading to strongly improved activity for the generation of $^{\bullet}OH$ radicals, but also generates surface defects in the materials. The defective sites act as electron traps, which depress the photocatalytic hydrogen evolution activity. However, by combining ball milling and photodeposition of Rh, highly improved hydrogen generation rates for $CsTaWO_6$ are achieved. The sol–gel citrate route finally leads to more active materials than the solid state reaction.

1. Introduction

Converting solar energy into sustainable fuels is one of the main challenges scientists are facing nowadays.[1] Solar water splitting with semiconductor materials is an attractive approach for sustainable energy conversion using solar radiation.[2] Since the pioneering reports by Boddy and Fujishima describing photoelectrochemical water splitting by TiO_2,[3,4] numerous reports and reviews have appeared in the last decades that describe active photocatalysts for clean hydrogen production and direct water splitting, including TiO_2, Ta_2O_5, Nb_2O_5, WO_3 and Ga_2O_3.[5–9]

TiO_2 has been one of the most investigated photocatalysts due to its high activity, low toxicity and low cost.[10,11] However, the large band gap values (E_g) of anatase and rutile-type TiO_2 (3.2 and 3.0 eV, respectively) impair the utilisation of visible light that comprises *ca.* 43% of the solar spectrum. Consequently, many research groups are searching for alternative photoactive materials with band gaps below 3 eV in order to more effectively utilise visible light in photocatalysis.

Another highly investigated material for energy applications including electrochromic applications,[12] photoelectrochemistry and photocatalysis is WO_3. Like TiO_2, WO_3 is very stable and is active towards water oxidation, as was first reported in 1976.[13] Additionally, WO_3 has a lower E_g than TiO_2, lying between 2.4–2.8 eV,[14–16] enabling it to harness longer-wavelength light for photocatalysis. However, due to its conduction band (CB) minimum being more positive than the standard hydrogen potential (+0.5 V *vs.* NHE),[17] no spontaneous hydrogen generation and overall water splitting can be achieved with pure WO_3.

To tune the electronic structure and shift the conduction band upwards to achieve photocatalytic hydrogen generation, WO_3 can be fused with other metal oxides to form binary or ternary tungstates.[18] One promising example is $CsTaWO_6$, which crystallises to form the defect-pyrochlore structure, and was first reported to be photocatalytically active under UV light (E_g = 3.8 eV) by Ikeda *et al.*[19] Very recently, the group of Lu *et al.* demonstrated that $CsTaWO_6$ can generate hydrogen from aqueous solutions containing 20% ethanol without any co-catalyst under solar irradiation.[20] Moreover, the crystal structure of $CsTaWO_6$ was found to be well suitable for homogeneous anion doping with nitrogen and/or sulfur, which readily incorporate as anions into the lattice of $CsTaWO_6$ and consequently reduce its band gap. $CsTaWO_6$ doped with nitrogen and/or sulfur exhibited remarkable red

[a]*Laboratory of Industrial Chemistry, Ruhr-University Bochum, Universitaetsstrasse 150, 44801 Bochum, Germany*
[b]*Institute for Chemistry, Carl-von-Ossietzky-University Oldenburg, Carl-von-Ossietzky-Strasse 9-11, 26129 Oldenburg, Germany*
[c]*Institute of Physical Chemistry, Justus-Liebig-University Giessen, Heinrich-Buff-Ring 58, 35392 Giessen, Germany. E-mail: roland.marschall@phys.chemie.uni-giessen.de; Fax: +49-641-9934509; Tel: +49-641-9934585*

† Electronic supplementary information (ESI) available: Additional X-ray diffraction patterns and hydrogen generation curves. See DOI: 10.1039/c3ra42768d

shifts of the absorption into the visible light range, and was highly active for hydrogen generation under sunlight irradiation, even without co-catalysts. Recent reports show the applicability of this strategy also to other photocatalyst materials with such open crystal structures like $Ba_5Ta_4O_{15}$ or $Sr_2Ta_2O_7$.[21–23]

Most mixed-oxide semiconductor materials used for photocatalysis are usually synthesised *via* solid state reaction (SSR), which involves mixing stoichiometric amounts of metal oxide and/or carbonates and heating them to temperatures between 800 and 1200 °C. However, various mixed metal oxides can be synthesised under milder conditions using sol–gel techniques like the polymerisable complex (PC) method[24,25] or the citrate route.[26] Using these sol–gel methods, photocatalytically active mixed oxide powders featuring smaller particle sizes and high crystallinity can be obtained at relatively low calcination times and temperatures compared to those required by SSR methods, yielding more efficient photocatalysts due to their higher surface areas and short charge carrier diffusion pathways.

In the present manuscript, we report the first sol–gel synthesis of $CsTaWO_6$ *via* an aqueous sol–gel route called the citrate route. Sol–gel-derived $CsTaWO_6$ was calcined over a wide range of temperatures and times to optimise its surface area, crystallinity and photocatalytic activity, all of which are compared to the properties of $CsTaWO_6$ prepared by conventional SSR. We also show that post-synthetic ball milling has a strong influence on the photocatalytic activity of $CsTaWO_6$ prepared by either SSR or sol–gel method towards terephthalic acid hydroxylation and hydrogen generation in the absence of a co-catalyst. Finally, we demonstrate the effects of photodeposition of co-catalyst onto ball-milled and as-synthesised (sol–gel or SSR) materials on photocatalytic hydrogen generation. These investigations lead to an optimised material amendable to future anion doping and hydrogen generation in visible light.

2. Experimental

Synthesis of materials

For the synthesis of $CsTaWO_6$ *via* citrate route, 7 g ethylenediaminetetraacetic acid (EDTA, 99%, Alfa Aesar) and 7.25 g citric acid (98%, Alfa Aesar) were dissolved in 570 mL water, the pH was adjusted to 8.3 using conc. ammonia (aq.) (33%, J. T. Baker). After dissolution, the pH was adjusted to 5 using conc. nitric acid (J. T. Baker), and 15 mL hydrogen peroxide was added to stabilise the highest oxidation states of Ta and W. Tantalum ethoxide ($Ta(OEt)_5$, Alfa Aesar) was dissolved in abs. ethanol, and added in small portions to the solution while heating to 90 °C. Then, ammonium tungstate ($(NH_4)_{10}(W_{12}O_{41})\cdot H_2O$, Aldrich) was added slowly. Finally, caesium nitrate ($CsNO_3$, Aldrich) was added to the clear solution. After solvent evaporation, a black powder precursor remains, which is calcined at different temperatures (600–900 °C) and for different times (4–36 h) to burn away residual carbon and induce crystallinity, yielding the final white product. A schematic representation of the citrate route synthesis is shown in Fig. 1.

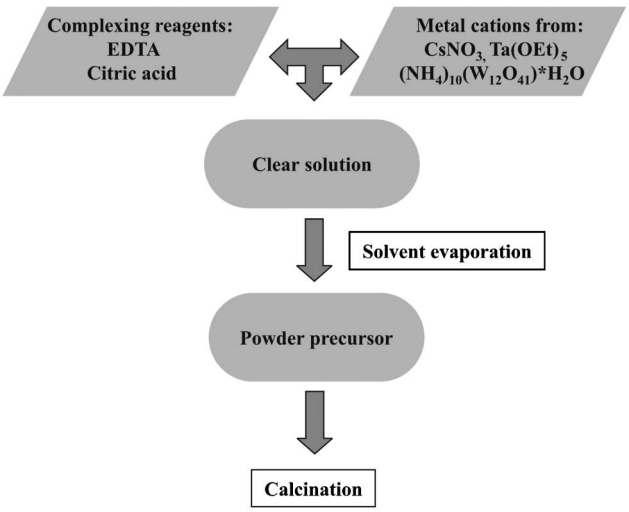

Fig. 1 Synthesis procedure for the citrate route to $CsTaWO_6$.

For the SSR synthesis, $CsTaWO_6$ was synthesised according to a literature procedure.[20] Briefly, stoichiometric amounts of caesium carbonate ($CsCO_3$, Aldrich), tantalum(v) oxide (Ta_2O_5, Aldrich) and tungsten(vi) oxide (WO_3, Aldrich) were mixed vigorously in a mortar and calcined at 810 °C for 36 h with one intermediate grinding after 18 h. Ball-milling of some citrate route and SSR-derived $CsTaWO_6$ samples was performed in a rotary ball mill (Spex Industries) with agate crucible and 2 agate balls (diameter 5 mm and 10 mm) for up to 10 min.

Characterisation

X-ray diffraction patterns were recorded on a PANalytical MPD diffractometer using Cu-Kα radiation (λ = 1.5406 Å) in the range of 10 to 70 degrees 2Θ. Brunauer–Emmett–Teller (BET) surface areas were measured by N_2 gas physisorption isotherms with a Quantachrome Autosorb-1-MP. UV-Vis diffuse reflectance spectra were measured using a Perkin Elmer Lambda 650 UV-Vis spectrometer equipped with a Praying-Mantis mirror unit. The obtained spectra were converted by the Kubelka–Munk function, F(R), into absorption spectra, using $BaSO_4$ as a white standard. Optical band gaps (E_g) were obtained *via* Tauc-plot method[27–31] using the calculation $\alpha = A(h\nu - E_g)^n/h\nu$, where α is the absorption coefficient, A is a constant, $h\nu$ is the energy of light, and n = 2 or 0.5 is used for materials with indirect or direct transition, respectively. Assuming that the absorption coefficient α is proportional to the Kubelka–Munk function $F(R)$, the E_g can be obtained from the plot of $[F(R)h\nu]^{1/n}$ *versus* $h\nu$, by extrapolation of the linear part near the onset of the absorption edge to intersect the energy axis.

Photocatalytic activity tests

The amount of photogenerated ·OH radicals upon irradiation was measured according to a literature method.[20] 500 mg photocatalyst was suspended in 500 mL solution containing 0.01 M NaOH and 3 mM terephthalic acid (TA, 98%, Aldrich).

The suspension was stirred in the dark for 30 min, and then illuminated using a 150 W Xe immersion lamp (Peschl UV Consulting). Samples of 5 mL were taken every 15 min and filtered before taking fluorescence measurements (Horiba Jobin Yvon FL322 Fluorolog-3-system). Upon irradiation, the photogenerated ·OH radicals react with TA to form 2-hydroxyterephthalic acid (TAOH), which shows a characteristic fluorescence band at 426 nm.[32] An increase in intensity with time is thereby directly related to an increased concentration of photogenerated ·OH radicals. The applied excitation wavelength was 320 nm.

Photocatalytic hydrogen generation was measured in a home-built, air-free closed gas system using a typical double-walled inner irradiation-type quartz reactor comparable to those described in the literature.[33] As a light source, a 700 W Hg mid-pressure immersion lamp (Peschl UV-Consulting, set to 50% power = 350 W) was used for irradiation and cooled to 10 °C with a double-walled quartz mantle using a thermostat (LAUDA). Gas evolution was measured online using a multi-channel analyser (Emerson) equipped with a detector for the determination of the concentration of hydrogen (thermal conductivity detector), oxygen (paramagnetism) and carbon dioxide (IR). Argon 6.0 was used as a carrier gas, the continuous gas flow was controlled by a Bronckhorst mass flow controller. The gas flow was set to 50 NmL min^{-1}. All reactions were performed at 13 °C.

400 mg photocatalyst was suspended in 460 mL water and 40 mL methanol. Before photocatalytic reactions were initiated, the whole system, with the photocatalyst included, was flushed with Argon 6.0 at 100 NmL min^{-1} for approx. 30 min to remove any trace of air.

Metallic Rh was deposited onto the photocatalysts *via* reductive photodeposition[34] using a 1.3 mM Na_3RhCl_6 (99.999%, Aldrich) solution as the precursor for loading of the co-catalyst.[33,35] Before adding the Rh salt solution, the light irradiation was stopped and the precursor solution was added *via* syringe through a rubber seal without opening the reactor. Traces of air were subsequently removed by flushing the reactor again with Argon before starting light irradiation. Upon light irradiation, metallic Rh is preferentially deposited onto more electron-rich photocatalyst surface sites. During Rh photodeposition, CO_2 derived from catalytically oxidised methanol was also detected with our gas analyser. Gas evolution measurements were continued to determine the hydrogen generation activity of the Rh-modifed $CsTaWO_6$, still using methanol as the sacrificial reducing agent. Measurements were repeated several times, the error is <10 μmol h^{-1}.

3. Results and discussion

Characterisation

Fig. 2a shows the X-ray diffraction (XRD) patterns of the sol–gel-derived $CsTaWO_6$ powder precursors calcined at different temperatures for 10 h, as well as those for the SSR product. The reflections of the SSR product indicate a highly crystalline material, and the XRD pattern is in perfect agreement with

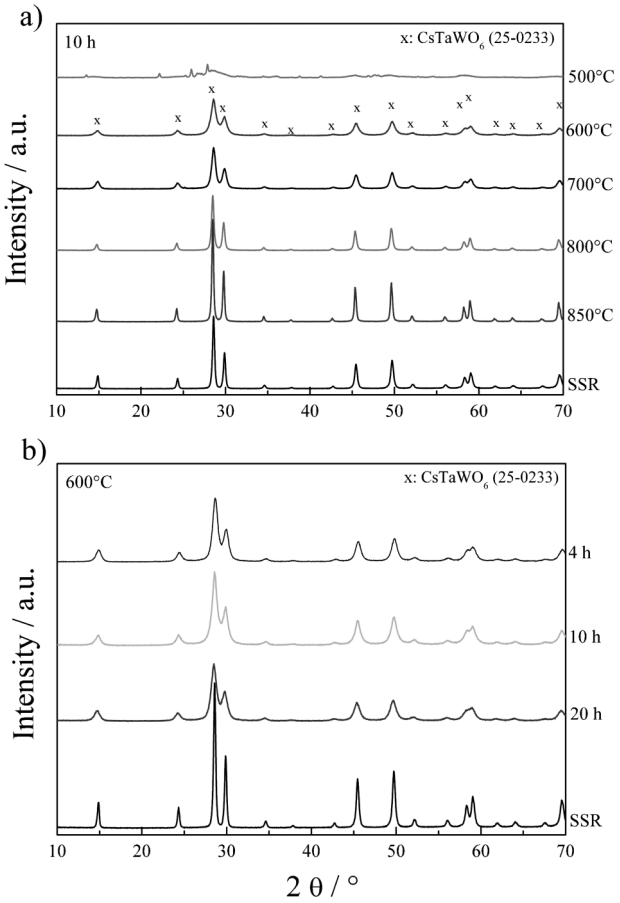

Fig. 2 XRD patterns determined after (a) 10 h calcination at different temperatures; (b) after calcination at 600 °C for different times.

previously published $CsTaWO_6$ XRD data[19,20] and the standard diffraction pattern of $CsTaWO_6$ (JCPDS 25-0233). The defect-pyrochlore structure of $CsTaWO_6$ consists of corner-sharing TaO_6 and WO_6 octahedra, forming a three-dimensional framework possessing tunnels with hexagonal cross-section down the *c*-axis, in which the Cs cations are located on the crystallographic 8b sites.[36] After calcination of the powder precursor derived from the citrate route at 500 °C, few reflections indicating crystalline $CsTaWO_6$ are visible in the XRD patterns. However, after calcination for 10 h at 600 °C, all reflections for the defect-pyrochlore structure are already visible, and no impurities are evident. The reflections are very broad compared those for the SSR product, which indicates that the sol–gel product features a small particle size. The SEM and TEM images (Fig. 3) further confirm that the citrate route product consists of much smaller primary particles (<50 nm) than the SSR product (several 100 nm).[20] However, the SEM images show that the citrate route particles tend to form sponge-like agglomerates with big cavities, which is also the reason for the only little increase in surface area (Table 1). With increasing calcination temperature, the XRD reflections in Fig. 2a become narrower and increase in intensity, which indicates increasing crystallinity and particle growth due to sintering. Fig. 2b shows the effect of calcination time on the

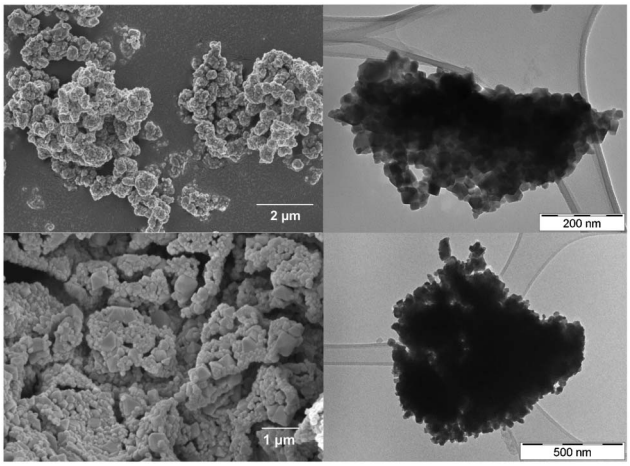

Fig. 3 SEM pictures of $CsTaWO_6$ after SSR (upper left) and sol–gel synthesis calcined for 10 h at 850 °C (lower left); TEM pictures (right) of $CsTaWO_6$ calcined for 20 h at 850 °C.

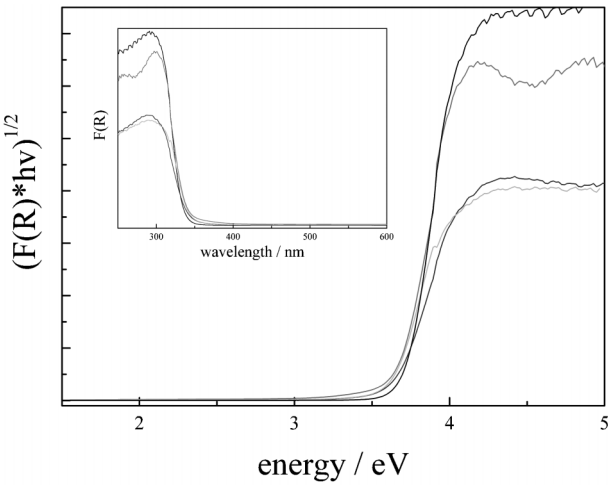

Fig. 4 Kubelka–Munk spectra (inset) and Tauc plot of 4 exemplarily chosen synthesis pathways: SSR (black), 4 h @ 600 °C (dark grey), 10 h @ 800 °C (grey), 20 h @ 850 °C (light grey).

crystallinity of $CsTaWO_6$. At 600 °C, the crystallinity of the samples does not change distinctly over time and a well-crystallised material is already obtained after calcination of sol–gel-derived $CsTaWO_6$ for only 4 h. The calcination temperatures and times necessary to crystallise citrate route-derived $CsTaWO_6$ are remarkably low in comparison to the long reaction times and high reaction temperatures required to obtain $CsTaWO_6$ *via* SSR.[19] Although the trend is barely visible when calcining at 600 °C, at temperatures >600 °C our materials become markedly more crystalline with increasing calcination time. The XRD reflections increase in intensity with calcination time, as exemplarily shown for the citrate route product calcined at 850 °C (supplementary information,† Fig. SD1). The effects of a wide range of calcination times and temperatures on the crystallinity of sol–gel-derived $CsTaWO_6$ are summarized by the XRD data in Fig. 2a and 2b. The data reveal that the calcination temperature has the bigger influence of the two variables on the crystallinity of the sol–gel materials. We also calculated the mean primary particles sizes using the Scherrer equation to confirm this trend. The particles sizes increase from ~23 nm to ~50 nm by increasing the calcination temperature from 600 °C to 850 °C, while only minor changes are observed at 850 °C when the calcination time was varied from 5 h to 20 h (50–55 nm).

Fig. 4 shows the absorption spectra and the Tauc plots of $CsTaWO_6$ prepared with different calcination temperatures and times, as well as that for the SSR product. All materials exhibit nearly the same band gap of *ca.* 3.6 eV, which is slightly smaller than the reported literature values.[19,20] Although the materials therefore still require UV irradiation in order to generate charge carriers, $CsTaWO_6$ derived from the SSR is a very good photocatalyst for visible light hydrogen generation after suitable post-synthetic anion doping,[20] and sol–gel-derived $CsTaWO_6$ should be similarly amenable to anion doping. While this investigation primarily describes the first successful sol–gel low temperature synthesis of this defect-pyrochlore photocatalyst, $CsTaWO_6$, and the factors influencing its performance, different anion doping experiments will be pursued in the future to extend the absorption of the optimised sol–gel photocatalysts.

Table 1 Surface area and H_2 production (with co-catalyst Rh) of different $CsTaWO_6$ samples

$CsTaWO_6$	Specific surface area/m^2 g^{-1}	H_2 production[a]/ μmol h^{-1}
SSR	2,2	651
SSR-BM	3,9	769
20 h 850 °C	2,2	742
20 h 850 °C BM	5,1	828
10 h 850 °C	3,3	743
10 h 850 °C BM	3,9	648
36 h 810 °C	1,5	406
36 h 810 °C BM	4,8	506

[a] 0.4 g photocatalyst, 460 mL water, 40 mL methanol, 350 W Hg mid-pressure lamp, inner-irradiation setup, Ar carrier gas, 0.075 wt.-% Rh; BM = after 10 min ball milling.

Terephthalic acid hydroxylation

The sol–gel synthesis of $CsTaWO_6$ and the small particle size of the as-prepared materials have a strong influence on the photocatalytic activity of the materials. We used the photocatalytic hydroxylation of terephthalic acid (TA) to investigate the ability of the photocatalysts to generate holes in its valence band (VB) under broad-spectrum (including UV) illumination. Photogenerated holes can react with surface adsorbed water to generate highly reactive ·OH radicals which can be used to decompose *e.g.* organic pollutants. These radicals also can react with TA to form 2-hydroxy terephthalic acid (TAOH), which emits a characteristic fluorescence at 426 nm.[20,32]

Fig. 5a (inset) shows the TAOH fluorescence signals arising upon irradiation of a $CsTaWO_6$ (SSR) suspension in TA/NaOH with a 150 W Xenon immersion lamp. With progressive irradiation time the fluorescence signal increases, indicating an increased amount of TAOH formed in the suspension.

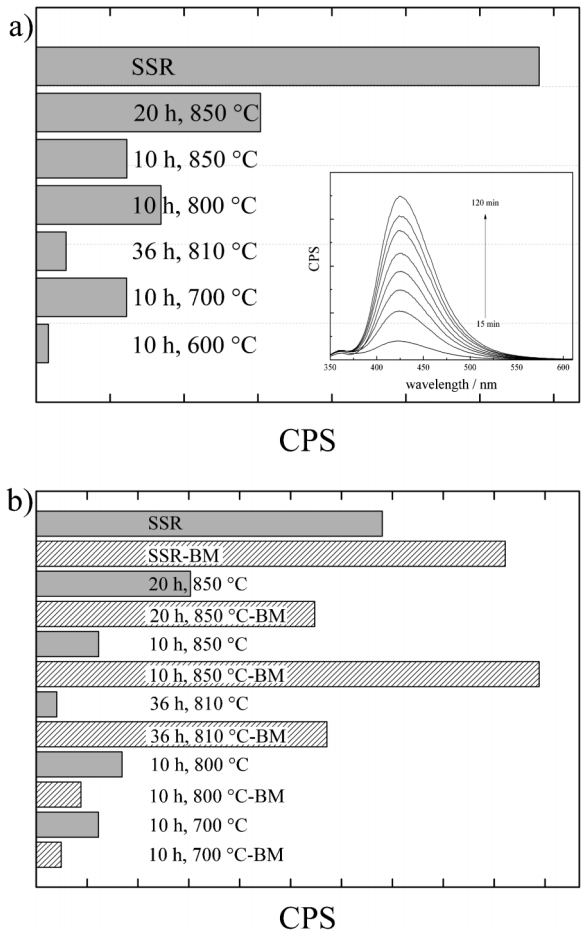

Fig. 5 (a) Fluorescence spectra of UV light irradiated $CsTaWO_6$ suspension in 3 mM terephthalic acid at different irradiation times (inset), and maximum intensities (at 426 nm) after 120 min irradiation for different prepared samples; (b) maximum intensities after 120 min irradiation of different prepared samples compared to ball-milled samples.

Thus, positive charge carriers are generated in the VB of the photocatalyst upon irradiation, which react with surface water to form ·OH radicals, which then react with TA to generate TAOH. The linear increase of fluorescence intensity with time indicates good material stability. Fig. 5a also shows the fluorescence intensities at 426 nm after 120 min for different $CsTaWO_6$ samples. $CsTaWO_6$ prepared *via* SSR reaction exhibited the highest activity in this photocatalytic reaction, even though the sol–gel product calcined for 20 h at 850 °C has a higher degree of crystallinity (Fig. 2a). The specific surface area of the SSR product was 2.2 $m^2\ g^{-1}$; the materials derived from the sol–gel citrate route exhibit comparable specific surface areas (Table 1). Additionally, with appropriate calcination time the activity of our sol–gel materials improves substantially. Samples calcined at 850 °C for 20 h have the highest activity among our sol–gel products, although the specific surface area decreases from 3.3 to 2.2 $m^2\ g^{-1}$ after increasing the calcination time at 850 °C from 10 to 20 h. Presumably the increased degree of crystallinity achieved at the longer calcination time greatly improves the photocatalytic process, such that the photocatalytic activity more than doubles after the longer calcination time in spite of a *ca.* 33% loss in specific surface area. Similarly, sol–gel-derived $CsTaWO_6$ calcined at 600 °C, which featured the poorest crystallinity of all of the catalysts tested for photocatalytic activity, exhibits very low activity. After calcination at 700 °C, however, the activity increases >6-fold, which is again due to increased crystallinity.

We also prepared a $CsTaWO_6$ sample *via* sol–gel citrate route using calcination time and temperature comparable to those used in the SSR procedure, producing a photocatalyst with very low activity. The long calcination time of 36 h yields highly crystalline, but also highly sintered $CsTaWO_6$ particles and a substantially reduced specific surface area (1.5 $m^2\ g^{-1}$), leading to dramatically decreased activity. Excessive calcination times (*e.g.* 36 h) and temperatures higher than 850 °C produce materials with severely diminished activities. Sol–gel-derived $CsTaWO_6$ calcined for 10 h at 900 °C (not shown) has negligible photocatalytic activity for terephthalic acid hydroxylation, further supporting this conclusion.

In order to break up the large, micrometer-scale agglomerates that form during the sol–gel citrate route preparation of $CsTaWO_6$ (Fig. 3), we performed short tribochemical treatments using a ball mill. Comparison of the XRD patters before and after ball milling reveals that the procedure has no effect on the crystal structure of our materials (Supplementary Information† Fig. SD02). However, the activity for photocatalytic TA hydroxylation increases substantially after 10 min of ball milling for all samples calcined at temperatures higher than 800 °C (Fig. 5b). Additionally, due to the morphology of the sol–gel-derived $CsTaWO_6$ after calcination, the effect of ball milling on their activity is much more pronounced than for $CsTaWO_6$ prepared by the SSR. Ball milling breaks up the sponge-like agglomerates, thereby increasing the accessible surface area. This can also be seen in SEM images taken after ball milling (Fig. SD03, ESI†) in comparison to Fig. 3. The tribochemical treatment enlarges the specific surface area of all samples, even of the SSR product (Table 1). The largest increase in specific surface area occurs in the sol–gel product calcined for 36 h at 810 °C (this sample was prepared under comparable heating conditions to those in the SSR synthesis), increasing more than three fold, from 1.5 to 4.8 $m^2\ g^{-1}$. The activity of this sample for TA hydroxylation increases 14-fold after ball milling, which is also the highest increase in TA hydroxylation activity among all samples. The citrate route product calcined for 10 h at 850 °C also exhibits a large (8-fold) increase in activity after ball-milling, while the already-larger specific surface area for this sample (3.3 $m^2\ g^{-1}$) increased more modestly (by <20%) to 3.9 $m^2\ g^{-1}$. This sample, after ball milling, is the most active material for TA hydroxylation, even better than the ball-milled SSR product.

The surface area clearly has a significant effect on the TA hydroxylation activity, but crystallinity is an equally and perhaps more critical variable. When only calcination temperatures and times are varied, the relationship between TA hydroxylation activity and material specific surface area change is complicated by these competing effects. This competition is evident in the lack of clear trends in measured TA activities in Fig. 5a and the measured specific surface areas for the non-ball-milled samples in Table 1. The tribochemical

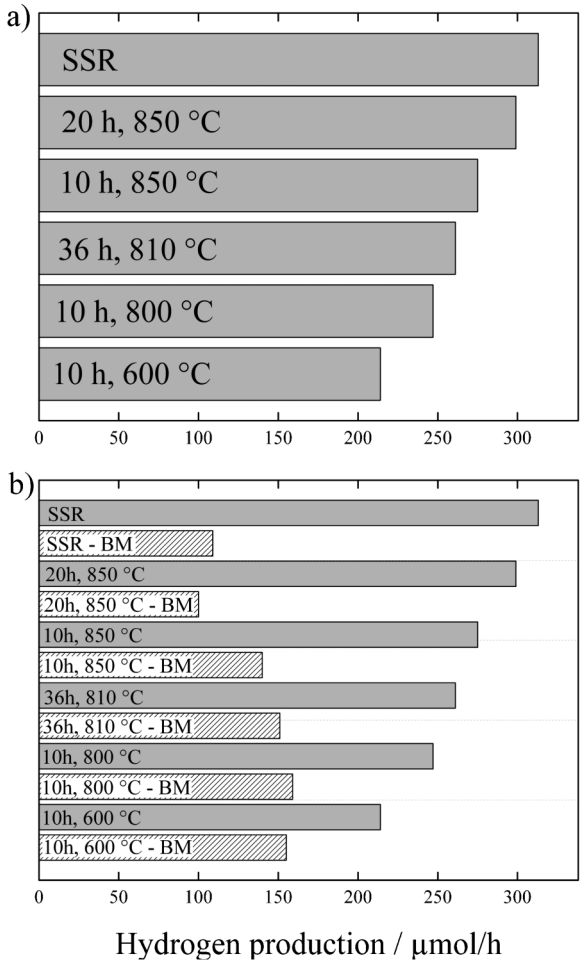

Fig. 6 (a) Hydrogen production without co-catalyst from water/8% methanol solution for $CsTaWO_6$ prepared *via* different synthesis routes; (b) effect of 10 min ball milling on hydrogen production (dashed) without co-catalyst.

treatment provides a partial solution to this complication, as the activities of all materials for TA hydroxylation increases after ball milling, but the increase in activity compared to that in surface area varies substantially. For example, the sol–gel samples after 20 h calcination at 850 °C show a distinct increase in specific surface area after ball milling, from 2.2 to 5.1 $m^2\ g^{-1}$, but the activity for TA hydroxylation only doubles. Thus, other effects must play a role in the photocatalytic activity of our materials, which will be shown in the next part. Despite these complications, short-time ball milling is a simple method that significantly improves TA hydroxylation, as it opens the particle agglomerates after sol–gel synthesis, leading to improved specific surface areas and TA hydroxylation activities of $CsTaWO_6$ in all cases.

Photocatalytic hydrogen production

As a second photocatalytic evaluation we investigated the hydrogen generation capability of our materials, since $CsTaWO_6$ is known to be a very good hydrogen generation photocatalyst.[19,20] As shown in Fig. 6a, $CsTaWO_6$ prepared *via* different synthesis routes and calcination procedures generate hydrogen from alcoholic solutions without the need for a co-catalyst. These results are in agreement with those reported elsewhere,[20] however the active surface sites for this reaction are not yet known. The activity of sol–gel-derived $CsTaWO_6$ increases with calcination temperature and time, and thereby with crystallinity, and calcination temperature has a bigger influence than calcination time. Without co-catalyst, the SSR product exhibits a slightly higher activity than the sol–gel products for hydrogen production, but these differences deriving from the synthesis method are relatively minor.

Since ball milling had such a large effect on the photocatalytic TA hydroxylation activity of our materials, we also performed hydrogen production experiments with ball-milled $CsTaWO_6$. In contrast to the TA hydroxylation results, ball milling has a very negative effect on the photocatalytic hydrogen generation activity of $CsTaWO_6$ without co-catalyst, independent of the synthesis procedure. Hydrogen evolution rates decrease substantially for all samples after ball milling (Fig. 6b). The contrast between the changes in TA hydroxylation and H_2 generation activity of $CsTaWO_6$ before and after ball milling may derive from surface defects created during ball milling, which can act as electron traps.

Ball milling increases the surface area of $CsTaWO_6$, especially of our sol–gel products (Table 1). The tribochemical treatment had a positive effect on activity of $CsTaWO_6$ for photocatalytic TA hydroxylation because increasing the surface area directly increases the probability that positive charge carriers generated in the VB during illumination can reach the surface and generate $^{\bullet}OH$ radicals by oxidising surface-adsorbed water, which then react with TA. In contrast, in hydrogen generation reactions the negative charge carriers photoexcited into the conduction band of $CsTaWO_6$ are the primary reactive species in the initiation of the catalytic reaction pathway. Therefore the negative effect of ball milling must be related to the electron pathway in the photocatalytic reaction (*e.g.* the energetics and/or recombination kinetics of the photogenerated electron), not only to surface area effects. Surface defects acting as electron traps may divert photogenerated electrons from sites that are active for the catalytic reduction of water, thus decreasing H_2 generation rates. While the evidence for the generation of surface defects by short time ball milling that act as electron traps is indirect, such a mechanism is a reasonable explanation for the decreased hydrogen generation activity in the absence of a co-catalyst.

We have tried to investigate the nature or type of the formed defects by XPS, but no changes in surface composition were found, giving no indication for general creation of point defects. Local defects due to the reduced agglomerate size and the increased surface area might not have been detected. Additional Raman investigations before and after ball mill of representative SSR and sol–gel samples did also not give rise to any new modes which would indicate the formation of defects upon ball milling (Fig. SD04, ESI†). All appearing modes are according to literature.[37] Only slight shifts of some Raman modes can be observed, which might be due to tension created inside the crystal structure, however more detailed investigations are needed to confirm these results.

The influence of ball milling also depends on the intrinsic materials properties. The decrease in activity for sol–gel-

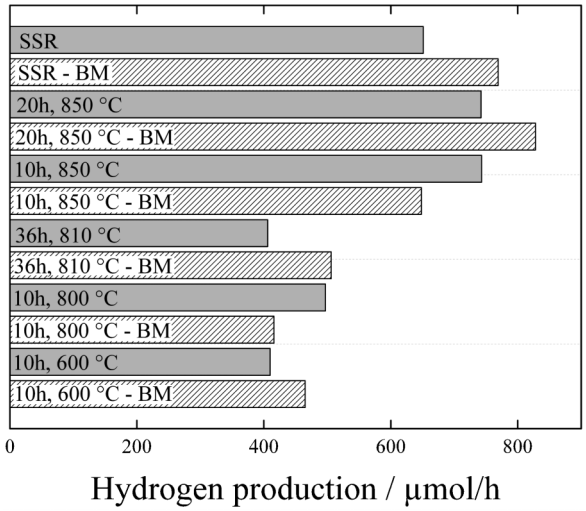

Fig. 7 Hydrogen production rates from water/8% methanol solutions with calcined samples after photodeposition of 0.075 wt.-% Rh (grey), compared to additionally ball-milled samples decorated with 0.075 wt.-% Rh (dashed).

derived $CsTaWO_6$ samples is more pronounced for samples with higher crystallinity (Fig. 6b). Samples calcined at low temperatures suffer less pronounced decreases in activity than the samples calcined at 850 °C. Ball milling of highly crystalline $CsTaWO_6$ creates surface defects on materials that have few defects initially, thus the fractional increase in defect concentration after ball milling is high. In contrast, samples with low crystallinity have already many defects, so the relative change in concentration of surface defects after ball milling is lower. Such changes in relative surface defect concentration may explain the corresponding changes in the hydrogen generation activity of the ball-milled $CsTaWO_6$ samples.

As mentioned before the electron traps at the freshly formed surfaces are in concurrence to the sites at which hydrogen is formed, but their presence positively influences the TA hydroxylation activity after ball milling. Negative charge carriers trapped in surface states should be less likely to undergo recombination, extending the lifetimes of positive charge carriers available for TA hydroxylation, leading to the highly improved activities (Fig. 5b). Trapping effects could be at least partially responsible for the monotonic but nonlinear relationship between the increasing surface areas and increasing TA hydroxylation after ball-milling of the $CsTaWO_6$ photocatalysts.

The negative effect on the hydrogen generation should be negated or reversed by depositing Rh co-catalyst onto the photocatalysts surface, since metallic co-catalysts usually act as electron sinks for photoexcited charge carriers and as active sites for hydrogen production.[6,38] Fig. 7 shows the hydrogen production rates after Rh photodeposition before and after ball milling. First, its can be seen that after Rh deposition, the hydrogen evolution rates of the non ball-milled samples increase as expected compared to the pure $CsTaWO_6$ samples (Fig. 6a).

The hydrogen production rates more than double, reaching a maximum of 743 μmol h^{-1} for the non ball-milled sol–gel sample calcined for 10 h at 850 °C. It is also clear that the sol–gel materials calcined at 850 °C exhibit superior hydrogen production relative to that of the SSR products. As described earlier, a highly crystalline $CsTaWO_6$ powder can be obtained *via* the SSR, but a comparably crystalline $CsTaWO_6$ powder with improved surface area and smaller particle size can be synthesised *via* sol–gel method as long as the correct processing conditions are applied. Insufficiently low calcination temperatures yield an insufficiently crystalline sol–gel product, as observed for samples calcined below 850 °C (Fig. 7), and exceedingly long calcination times also lead to decreased activity (*e.g.* 36 h calcination). These effects on the hydrogen evolution were already apparent without addition of the Rh co-catalyst, but become even more pronounced after Rh deposition.

By photodeposition of Rh onto our ball-milled samples, the diminution of hydrogen production rates after ball milling is negated and the rates in most cases even improve compared to those of the non-ball-milled photocatalysts. The hydrogen production rates for all ball-milled defect-pyrochlores are much higher after Rh photodeposition (compare Fig. 6b and 7). This might indicate that the Fermi level of the Rh co-catalyst is energetically favoured compared to the proposed generated surface electron traps, lying at a more positive potential. Additionally, Rh is photodeposited at $CsTaWO_6$ surface sites preferentially where electrons accumulate, which are in this case the surface electron traps. Thus, the migration of photoexcited electrons to the co-catalyst Rh is highly promoted, leading to improved H_2 evolution rates. For example, the sol–gel product after 20 h calcination at 850 °C produces only 100 μmol h^{-1} hydrogen after ball milling, decreased from 299 μmol h^{-1}. But after photodeposition of 0.075 wt.-% Rh, the hydrogen production rate increased by 700% to 828 μmol h^{-1}. This rate is 11% higher than for the Rh decorated sample without ball milling, demonstrating that the tribochemical treatment has a strong but complex effect on hydrogen evolution at semiconductor photocatalysts. It is also the highest rate among all samples, even higher that the SSR sample, proving that *via* sol–gel citrate route a more crystalline and more active photocatalyst material can be prepared after much shorter synthesis time.

4. Conclusions

A facile synthesis approach to produce the highly crystalline and highly active mixed-oxide photocatalyst $CsTaWO_6$ *via* aqueous sol–gel citrate route was presented. The crystallinity of both SSR and sol–gel-derived $CsTaWO_6$ was dependent on calcination time and temperature, with the sol–gel route yielding materials with smaller primary particle sizes and improved specific surface area. The agglomerates that formed during sol–gel synthesis were tribochemically treated, leading to improved surface areas and highly improved photocatalytic activities for the oxidative generation of OH radicals for all of the $CsTaWO_6$ materials, which had been systematically calcined at different combinations of temperatures and times. Ball milling however generates surface defects that appear to

act like electron traps, resulting in decreased activities for hydrogen generation. All $CsTaWO_6$ samples generate hydrogen from water/8% methanol solutions without any co-catalyst, but combining ball milling and photodeposition of Rh resulted in the highest hydrogen production rates up to 828 μmol h^{-1} for the optimum sol–gel sample. This tribochemical approach should be easily transferable to other mixed oxide photocatalysts prepared *via* sol–gel or hydrothermal routes,[7] significantly improving their photocatalytic activities and leading to optimised materials for anion doping and hydrogen generation under visible light illumination.

Acknowledgements

We thank Dr Jeremy J. Pietron from the US Naval Research Laboratory, Washington, DC for his helpful comments and very fruitful discussions. We also thank Christian Suchomski (Justus-Liebig-University Giessen) for very fruitful discussions. We thank Dr Harun Tueysuez and the MPI for Coal Reasearch for TEM measurements, Dr Thomas Reinecke (Faculty of Geosciences, Ruhr-University Bochum) for XRD measurements, Noushin Arshadi for adsorption measurements, and Prof. Martin Muhler and Dr G. Wilma Busser (Laboratory of Industrial Chemistry, Ruhr-University Bochum) for support. We also thank Kirsten Keppler (Faculty of Geosciences, Ruhr-University Bochum) for providing the ball milling setup, and Prof. Harald Krautscheid (University Leipzig) for the crystal structure visualisation. The project ''Sustainable Chemical Synthesis (SusChemSys) is co-financed by the European Regional Development Fund (ERDF) and the state of North Rhine-Westphalia, Germany, under the Operational Programme ''Regional Competitiveness and Employment'' 2007–2013. R.M. gratefully acknowledges funding in the Emmy-Noether program (MA 5392/3-1) of the German Science Foundation DFG.

Notes and references

1 N. S. Lewis and D. G. Nocera, *Proc. Natl. Acad. Sci. U. S. A.*, 2006, **103**, 15729.
2 N. S. Lewis, *Nature*, 2001, **414**, 589.
3 P. J. Boddy, *J. Electrochem. Soc.*, 1968, **115**, 199.
4 K. Honda and A. Fujishima, *Nature*, 1972, **238**, 37.
5 F. E. Osterloh, *Chem. Mater.*, 2008, **20**, 35.
6 A. Kudo and Y. Miseki, *Chem. Soc. Rev.*, 2009, **38**, 253.
7 X. Chen, S. Shen, L. Guo and S. S. Mao, *Chem. Rev.*, 2010, **110**, 6503.
8 W. Y. Teoh, J. A. Scott and R. Amal, *J. Phys. Chem. Lett.*, 2012, **3**, 629.
9 P. D. Tran, L. H. Wong, J. Barber and J. S. C. Loo, *Energy Environ. Sci.*, 2012, **5**, 5902.
10 M. R. Hoffmann, S. T. Martin, W. Choi and D. W. Bahnemann, *Chem. Rev.*, 1995, **95**, 69.
11 X. Chen and S. S. Mao, *Chem. Rev.*, 2007, **107**, 2891.
12 C. G. Granqvist, *Solid State Ionics*, 1992, **53–56**, 479.
13 M. A. Butler, R. D. Nasby and R. K. Quinn, *Solid State Commun.*, 1976, **19**, 1011.
14 S. J. Hong, S. Lee, J. S. Jang and J. S. Lee, *Energy Environ. Sci.*, 2011, **4**, 1781.
15 H. Zheng, J. Z. Ou, M. S. Strano, R. B. Kaner, A. Mitchell and K. Kalantar-zadeh, *Adv. Funct. Mater.*, 2011, **21**, 2175.
16 Y. P. Xie, G. Liu, G. Q. (Max) Lu and H. M. Cheng, *Nanoscale*, 2012, **4**, 1267.
17 R. Abe, H. Takami, N. Murakami and B. Ohtani, *J. Am. Chem. Soc.*, 2008, **130**, 7780.
18 C. Janáky, K. Rajeshwar, N. R. de Tacconi, W. Chanmanee and M. N. Huda, *Catal. Today*, 2013, **199**, 53.
19 S. Ikeda, T. Itani, K. Nango and M. Matsumura, *Catal. Lett.*, 2004, **98**, 229.
20 (*a*) A. Mukherji, R. Marschall, A. Tanksale, C. Sun, S. C. Smith, G. Q. Lu and L. Wang, *Adv. Funct. Mater.*, 2011, **21**, 126; (*b*) R. Marschall, A. Mukherji, A. Tanksale, C. Sun, S. C. Smith, L. Wang and G. Q. Lu, *J. Mater. Chem.*, 2011, **21**, 8871.
21 A. Mukherji, C. Sun, S. C. Smith, G. Q. Lu and L. Wang, *J. Phys. Chem. C*, 2011, **115**, 15674.
22 A. Mukherji, B. Seger, G. Q. Lu and L. Wang, *ACS Nano*, 2011, **5**, 3483.
23 X. Zong, C. Sun, Z. Chen, A. Mukherji, H. Wu, J. Zou, S. C. Smith, G. Q. Lu and L. Wang, *Chem. Commun.*, 2011, **47**, 6293.
24 P. M. Pechini, *US Patent* 3330697, 1967.
25 M. Kakihana, *J. Sol-Gel Sci. Technol.*, 1996, **6**, 7.
26 J. Martynczuk, M. Arnold, H. Wang, J. Caro and A. Feldhoff, *Adv. Mater.*, 2007, **19**, 2134.
27 Y. Izumi, T. Itoi, S. Peng, K. Oka and Y. Shibata, *J. Phys. Chem. C*, 2009, **113**, 6706.
28 R. A. Van Leeuwen, C.-J. Hung, D. R. Kammler and J. A. Switzer, *J. Phys. Chem.*, 1995, **99**, 15247.
29 Y. Zhang, G. H. Li, Y. C. Wu, Y. Y. Luo and L. Zhang, *J. Phys. Chem. B*, 2005, **109**, 5478.
30 L. Bi and J. Y. Feng, *J. Lumin.*, 2006, **121**, 95.
31 I. Bannat, K. Wessels, T. Oekermann, J. Rathousky, D. W. Bahnemann and M. Wark, *Chem. Mater.*, 2009, **21**, 1645.
32 (*a*) Y. Zhao, W. Ma, Y. Li, H. Ji, C. Chen, H. Zhu and J. Zhao, *Angew. Chem., Int. Ed.*, 2012, **51**, 3188; (*b*) A. Y. Ahmed, T. A. Kandiel, T. Oekermann and D. W. Bahnemann, *J. Phys. Chem. Lett.*, 2011, **2**, 2461.
33 R. Marschall, J. Soldat, G. W. Busser and M. Wark, *Photochem. Photobiol. Sci.*, 2013, **12**, 671.
34 B. Kraeutler and A. J. Bard, *J. Am. Chem. Soc.*, 1978, **100**, 4317.
35 G. W. Busser, B. Mei and M. Muhler, *ChemSusChem*, 2012, **5**, 2200.
36 A. V. Knyazev, N. G. Chernorukov, N. N. Smirnova, N. Yu. Kuznetsova and A. V. Markin, *Thermochim. Acta*, 2008, **470**, 47.
37 M. Maczka, A. V. Knyazev, A. Majchrowski, J. Hanuza and S. Kojima, *J. Phys.: Condens. Matter*, 2012, **24**, 195902.
38 A. A. Ismail, S. A. Al-Sayari and D. W. Bahnemann, *Catal. Today*, 2013, **209**, 2.